small methods
www.small-methods.com

Spectromicroscopy of Nanoscale Materials in the Tender X-Ray Regime Enabled by a High Efficient Multilayer-Based Grating Monochromator

Stephan Werner, Peter Guttmann, Frank Siewert, Andrey Sokolov, Matthias Mast, Qiushi Huang, Yufei Feng, Tongzhou Li, Friedmar Senf, Rolf Follath, Zhohngquan Liao, Kristina Kutukova, Jian Zhang, Xinliang Feng, Zhan-Shan Wang, Ehrenfried Zschech, and Gerd Schneider*

The combination of near edge X-ray absorption spectroscopy with nanoscale X-ray imaging is a powerful analytical tool for many applications in energy technologies, catalysis, which are critical to combat climate change, as well as microelectronics and life science. Materials from these scientific areas often contain key elements, such as Si, P, S, Y, Zr, Nb, and Mo as well as lanthanides, whose X-ray absorption edges lie in the so-called tender photon energy range 1.5–5.0 keV. Neither conventional grazing incidence grating nor crystal monochromators have high transmission in this energy range, thereby yielding the tender photon energy gap. To close this gap, a monochromator setup based on a multilayer coated blazed plane grating and plane mirror is devised. The measurements show that this novel concept improves the photon flux in the tender X-ray regime by two-orders-of-magnitude enabling previously unattainable laboratory and synchrotron-based studies. This setup is applied to perform nanoscale spectromicroscopy studies. The high photon flux provides sufficient sensitivity to obtain the electronic structure of Mo in platinum-free $MoNi_4$ nanoparticles for electrochemical energy conversion. Additionally, it is shown that the chemical bonding of nano-structures in integrated circuits can be distinguished by the electronic configuration at the Si-K edge.

1. Introduction

Despite its enormous relevance for emerging energy conversion technologies, the tender X-ray regime is rarely exploited because of fundamental X-ray optical challenges. In contrast, the soft and hard X-ray regimes are extensively used at synchrotron radiation facilities based on monochromators with gratings[1,2] or crystals[3] to provide photon beams with high photon flux and high energy resolution for spectroscopy or microscopy.[4–6] Conventional plane grating monochromators (PGM) with a single layer coating are relatively inefficient in the tender X-ray range, and stray light is non-negligible due to a very shallow grazing angle of the incident photon beam. Crystal based monochromators operate in the tender regime under almost normal incidence conditions which causes heat load and thermal instabilities.

S. Werner, P. Guttmann, F. Siewert, A. Sokolov, M. Mast, G. Schneider
Helmholtz-Zentrum Berlin für Materialien und Energie
Elektronenspeicherring BESSY II
12489 Berlin, Germany
E-mail: stephan.werner@helmholtz-berlin.de

Q. Huang, Y. Feng, T. Li, Z.-S. Wang
Key Laboratory of Advanced Micro-Structured Materials MOE
Institute of Precision Optical Engineering
School of Physics Science and Engineering
Tongji University
Shanghai, 200092, P. R. China

The ORCID identification number(s) for the author(s) of this article can be found under https://doi.org/10.1002/smtd.202201382.

DOI: 10.1002/smtd.202201382

F. Senf
Institute for Physics and Astronomy
Potsdam University
14476 Potsdam, Germany

R. Follath
Paul Scherrer Institut
Villigen, 5232, Switzerland

Z. Liao, K. Kutukova, E. Zschech
Fraunhofer Institute for Ceramic Technologies and Systems
01109 Dresden, Germany

J. Zhang
Northwestern Polytechnical University
Xi'an, 710129, P. R. China

X. Feng
Technical University Dresden
Faculty for Chemistry and Food Chemistry
01067 Dresden, Germany

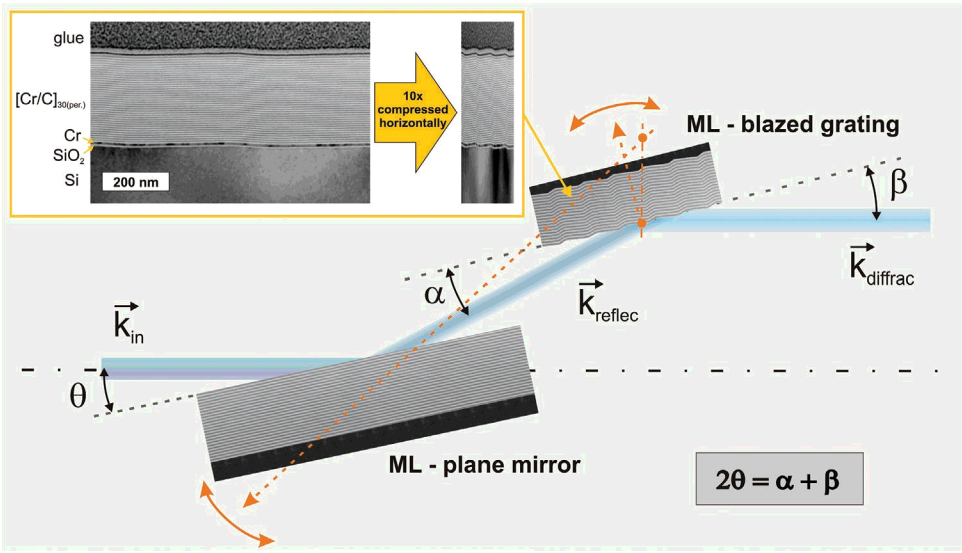

Figure 1. Schematic drawing of the optical monochromator setup at the U41-PGM1 beamline at BESSY II based on a multilayer coated blazed plane grating and mirror to improve the photon flux in the tender X-ray photon energy regime. The inset shows a TEM image of the cross-section of the Cr/C multilayer blazed grating structures. For better visualization of the grating period, the image was horizontally compressed 10 fold.

To overcome these limitations, we developed a volume Bragg-grating X-ray monochromator that consists of a blazed grating coated with a multilayer (ML) and a plane ML mirror operating under Bragg conditions. Electromagnetic theory predicts that volume diffraction effects of the 3D shape of the ML coated blazed grating results in high efficiencies.[7] Due to the extremely high precision with atomic accuracy of both ML periods to simultaneously fulfill the grating and the multilayer Bragg equation at the same time, it remained unclear whether this concept would work in practice. Here we show that the experimental difficulties can be overcome, and that this new ML monochromator concept based on volume diffraction yields a huge photon flux improvement, which enabled us to perform tender X-ray spectromicroscopy of nanoscale materials. Besides the enormous potential at synchrotron sources, our novel ML plane grating monochromator (ML-PGM) setup will also enable new capabilities in spectroscopy or microscopy applications at laboratory sources like higher harmonic generation (HHG). In addition, classical X-ray tube experiments requiring a small energy bandwidth will have dramatically reduced exposure times.

2. Multilayer Based Plane Grating Monochromator

The concept for the design of a ML coated blaze grating assumes that both the grating equation and the multilayer Bragg equation have to be fulfilled at the same time.[7] As illustrated in **Figure 1**, the incident beam with wave vector K_{in} and the diffracted light with wave vector K_{out} are parallel in an X-ray monochromator with pre-mirror for all transmitted wavelengths, which leads to the condition $2\theta = \alpha + \beta$. Combining the grating equation, the ML Bragg condition and taking refraction effects at the boundaries into account, we obtain for the period d_{ML} of the ML coating under the so called "on-blaze" operation mode:

$$d_{ML} = \frac{n}{m} d_{GR} \sin\gamma \frac{1}{\sqrt{1 - \frac{8\delta}{\lambda^2 m^2}(d_{GR}\sin\gamma)^2}} \quad (1)$$

with wavelength λ, grating period d_{GR}, blaze angle γ and diffraction orders for the grating m as well as the multilayer n. δ denotes the average refraction coefficient decrement of the ML material combination.[8] Although Equation 1 provides a first approximation, analytical theory based on a coupled wave approach has shown that a further ML period optimization should give the highest efficiency improvement.[9] Thus, even if Equation 1 yields d_{ML} = 5.5 nm, detailed theoretical studies revealed that a d-spacing of 5.9 nm should yield a higher transmission of the ML based monochromator (see more details in the Supporting Information).

However, due to the extremely demanding precision for the ML deposition process, no monochromator setups exist that have been equipped with ML coated blazed gratings and mirrors for applications in the tender photon energy range. To demonstrate the capability of this X-ray optical approach, we chose a combination of a blazed grating and a plane pre-mirror to be coated together by a Cr/C ML manufactured by magnetron sputtering (Figure S1, Supporting Information).

To test the efficiency of our new ML based monochromator setup, we incorporated it into the collimated plane grating monochromator (PGM) beamline at the undulator U41 at BESSY-II[10] (Figure S2, Supporting Information). In a first step we adjusted the tilt angles β and θ of both the ML blazed grating and the ML mirror based on values from efficiency and reflectivity measurements of the respective optics (Figures S3–S5,

E. Zschech
deepXscan GmbH
01067 Dresden, Germany
G. Schneider
Humboldt-Universität zu Berlin
Institut für Physik
12489 Berlin, Germany

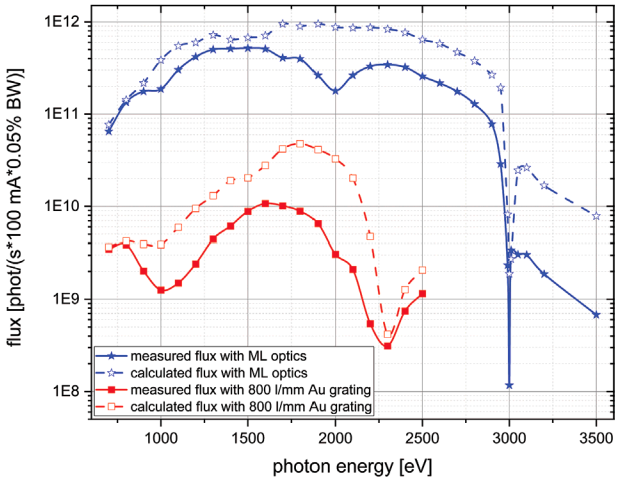

Figure 2. Comparison of the simulated and experimental X-ray photon flux for ML and Au coated optical elements at the U41-PGM1 monochromator beamline at BESSY-II. Experimentally, the photon flux for the ML based setup is increased by two-orders-of-magnitude. The magnification factor $c_{ff} = \cos\beta/\cos\alpha$ for the PGM is determined by the photon energy in the case of multilayer coated optical elements. For comparison, the c_{ff} values for the Au based PGM setup were chosen accordingly. Note, the photon flux drop close to 3 keV photon energy is due to the L_3 absorption edge of Rh which is the coating material of two additional mirrors in the beamline. The minimum in the photon flux curve for Au coated optics at around 2.2 keV is caused by the Au-M_5 absorption edge.

Supporting Information). The fine alignment of the monochromator setup was done by an optimization of the photon flux at each photon energy. These steps were repeated over the full photon energy range. Finally, an energy calibration of the beamline was performed with an ionization chamber containing sulfur hexafluoride (SF_6) gas. For this purpose, the sulfur K-absorption edge in the tender X-ray range was used (Figure S6, Supporting Information). In order to cover the full available photon energy range, we also checked the energy calibration at the neon and aluminum K-absorption edges. The measured photon flux of the ML based setup is shown in **Figure 2** (solid blue line). In order to compare the photon flux provided by the ML-PGM with the standard Au-PGM setup, we additionally measured the photon flux of the beamline equipped with standard Au coated optics[10] (Figure 2, solid red line). We observed a drastic photon flux increase by up to two-orders-of-magnitude for the ML-PGM. As a result, nanoscale spectromicroscopy is possible with significantly improved signal-to-noise ratio. Assuming that the X-ray photons are Poisson distributed an increase in photon flux by a factor 100 results in a 10 times better signal-to-noise ratio in the X-ray images.[11]

To better understand the contributions of the optical beamline components to the measured photon flux, we simulated the performance of the PGM monochromator beamline with an undulator source equipped with ML and Au optics (Figure 2, dashed lines). **Figure 3** illustrates the simulation workflow. The

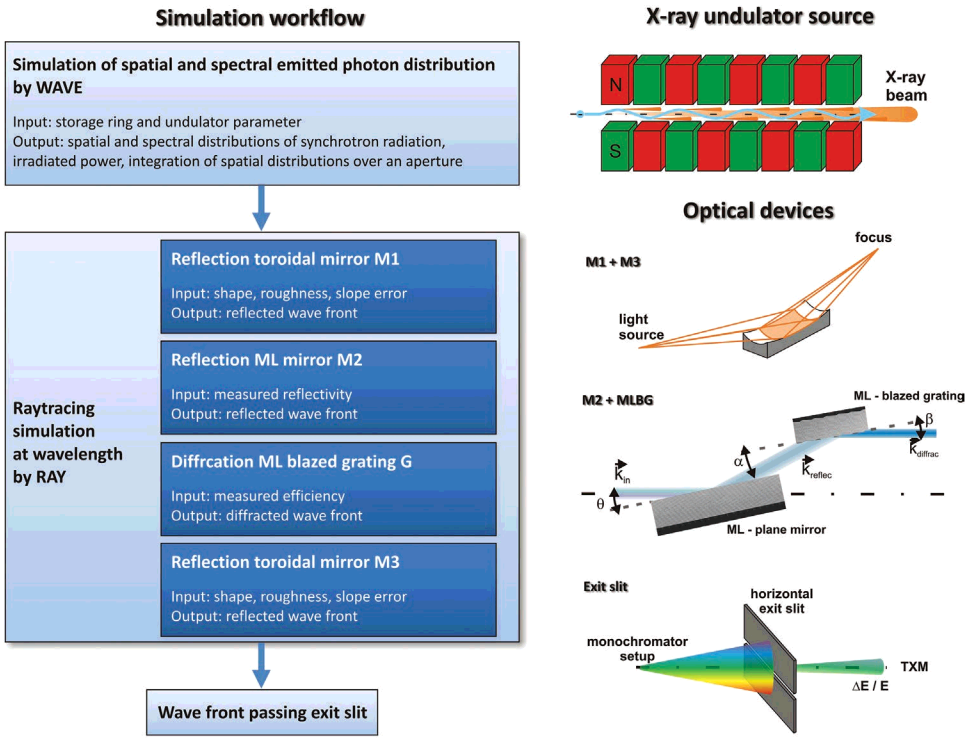

Figure 3. Scheme of the simulation workflow to calculate the photon flux of the ML based monochromator beamline at an undulator source. The emitted X-ray beam was simulated by the WAVE software package.[13] The raytracing of the X-ray propagation through the optical system of individual beamline components was performed by the RAY software package.[12] The right side shows the individual, optical elements of the beamline that are taken into account (see also Figure S2, Supporting Information).

simulation starts with the undulator source giving the emitted radiation for the illumination of the first beamline optic (mirror M1). Then, using raytracing accounting for the reflectivity and diffraction efficiency of the optical components of the U41-PGM1 beamline, we calculated the incident photon flux on the condenser of the X-ray microscope installed at approx. 9 m distance from the monochromator exit slit. The raytracing simulation was performed using the RAY software package (version 25.53),[12] while the emitted photons from the undulator were calculated by the WAVE software package (version 4.00/06).[13] The simulations accounted for imperfections in the optical components including roughness as well as slope errors, and the efficiency values of the standard Au plane grating and the ML blazed grating as well as the reflectivity of the Au and ML mirrors, which have been determined by actual measurements (Figures S3–S5, Supporting Information).

The experimental results for the photon flux shown in Figure 2 (solid lines) are in good agreement with the theoretical simulations (Figure 2, dashed lines), confirming that the new monochromator design is highly efficient in the tender photon energy range. The advantage of the ML setup arises mostly from the high efficiency of the ML blazed grating and the reflectivity of the ML mirror (see Figures S3 and S4, Supporting Information). The large drop in photon flux at ≈3 keV photon energy shown in Figure 2 is caused by the toroidal mirrors M1 and M3. Both mirrors are coated with rhodium having at 3 keV photon energy its Rh-L_3 absorption edge. The strong absorption in these mirrors explains the large loss in photon flux. Future beamlines designed to operate at higher photon energies will require different coating materials, for example a triple material combination of Pt, Cr, and B_4C. The increasing deviation of simulated and measured flux in the photon energy above 3 keV is also caused by a performance limitation of the current U41 undulator source. For the theoretical simulation of the emitted photon flux an ideal X-ray source was assumed. In practice, operation at photon energies above 3 keV requires very high harmonics of the undulator. This introduces imperfections and results in smaller emitted photon numbers in comparison to theoretical values. A further improvement of the beamline performance can be achieved by installing a new type of undulator source, for example an UE32 in-vacuum APPLE-II device,[14] which is under development. This undulator will provide higher photon flux at tender X-ray photon energies, as well as more flexibility regarding the polarization control of the X-ray beam. The potential of the presented ML-PGM concept can be further improved by using an increased number of ML bilayers in the ML grating and ML mirror. Theoretical calculations show that our ML based approach should provide high photon flux even in the wider photon energy range between 1 to 10 keV if the ML material is chosen accordingly (see Figure S7, Supporting Information) and the beamline is equipped with adapted optical elements and an improved undulator source is installed in a storage ring with higher electron energy.

3. Spectromicroscopy Studies using Tender X-Ray Photon Energies

Having demonstrated that the ML-PGM significantly improves the photon flux in the tender X-ray range, we coupled it with nanoscale transmission X-ray microscopy (TXM) to study advanced materials for catalysis and microelectronics. A grand challenge today is to identify efficient and robust systems for electrochemical energy conversion.[15] Advanced Mo- and Ni-based electrocatalysts have the potential to outperform conventional precious-metal-based materials (e.g., Pt-based precursors), given their electrocatalytic activity and long-term stability. In addition to the determination of the atomic structure of these catalysts using X-ray or electron diffraction techniques, it is critical for the understanding of their function to determine their electronic state, i.e., the particular type of chemical bonds that are formed. The electronic state can be predicted theoretically by density-functional theory with large efforts only, and traditional experimental approaches fail. Specifically, the electronic state of many advanced functional materials cannot be measured by electron energy loss spectroscopy (EELS) since the ionization energy of their constituent elements is too high for the acquisition of the respective ionization edges with sufficient intensity,[16] and furthermore most real catalyst particles are too thick for EELS measurements. Combined near edge X-ray absorption spectroscopy and transmission X-ray microscopy (NEXAFS-TXM; see optical setup in Figure S8, Supporting Information) at the Mo-L, Ni-L, and O-K absorption edges with high spatial resolution permits examination of the electronic structure of individual hierarchically structured catalyst components at the nanometre scale.

To demonstrate this, we used the described ML-PGM to investigate the chemical bonding in novel platinum-free $MoNi_4$ electrocatalyst nanoparticles under study for hydrogen evolution reaction in alkaline solutions. The nanoparticles were 20 to 100 nm in diameter and anchored on MoO_2 cuboids (see SEM images in Figure S9, Supporting Information). The cuboids had a rectangular cross-section of 0.5 × 1 μm^2 and lengths of 10 to 20 μm, and were aligned on conductive Ni foam ($MoNi_4/MoO_2$@Ni).[17] These nanoparticles were formed by controlling the outward diffusion of nickel atoms during annealing of precursor $NiMoO_4$ cuboids.[17,18] The coordination of Mo^{6+} ions of the precursor cuboids is octahedral in the α-$NiMoO_4$ phase, while it is tetrahedral in both the β-$NiMoO_4$ phase and the $NiMoO_4 \cdot nH_2O$ phase.[19] MoO_3 – a wide band gap semiconductor – is electrically insulating, and MoO_2 is electrically conductive.[20,21] The MoO_6 octahedrons in MoO_2 show a distortion with Mo-O bond lengths in the 1.97–2.07 Å range.[22,23]

To verify that the new ML-PGM permits spectromicroscopic studies at the Mo-L absorption edge, we compared spectral data acquired with the ML and the standard Au based monochromator setup (Figure S10, Supporting Information). We found that only the ML optics setup provides the required photon flux to extract valuable spectra, even if the exposure time is drastically increased and the monochromator exit slit is widened within an acceptable range using the standard Au optics. For a detailed study of the Mo- and Ni-based electrocatalysts, we determined NEXAFS spectra for $NiMoO_4$ cuboids and for MoO_2 cuboids with outdiffused $MoNi_4$ nanoparticles since the Mo-L NEXAFS of Mo-containing compounds (oxides, intermetallics) reveal the transition from Mo(2p) to Mo(4d) electronic states (**Figure 4**). For the metal oxides, they are sensitive to the oxidation state of Mo (see also Figures S11 and S12, Supporting

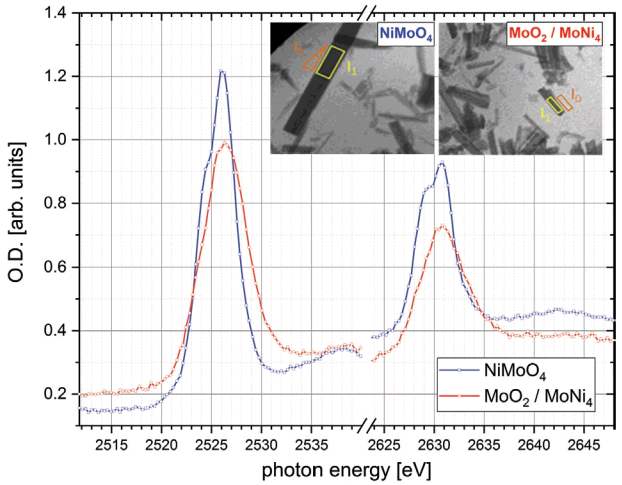

Figure 4. NEXAFS spectra at the Mo-L_{III} and Mo-L_{II} absorption edge extracted from energy series acquired on $NiMoO_4$ and MoO_2/$MoNi_4$ catalyst samples. Data were recorded at the U41-PGM1 monochromator beamline using ML-optics. The inset shows the corresponding sample regions of the X-ray microscopy images used for NEXAFS analysis.

Information).[24] The splitting of Mo-L features is caused by the metal-ligand interaction representing the Mo(4d) orbitals (e_g and t_{2g}), and it is an indication of the symmetry of the crystal structures.

With our new setup, we found for $NiMoO_4$ that the Mo-L_{II} absorption edge shows a main peak at 2630.8 eV and an additional shoulder at 2629.4 eV, while the Mo-L_{III} absorption edge shows a main peak at 2526.0 eV and an additional shoulder at 2524.6 eV (see Figure 4, blue graph). These observations demonstrate Mo(4d) orbital splitting of 1.4 eV at both the Mo-L_{II} and Mo-L_{III} edges (the Mo(4d) orbital splitting for α-$NiMoO_4$ with octahedral coordination is >3.0 eV). Furthermore, the shape of the peak/shoulder features (Mo-L_{II} features with a more pronounced shoulder than Mo-L_{III} features) are indications for tetrahedral coordination,[22] i.e., the mixed oxide is either hydrated $MoNiO_4$ or β-$NiMoO_4$.[19,25] X-ray diffraction (XRD) data of this sample published by Eda et al.,[26] Moura et al.,[27] Chen et al.,[28] and Du et al.[29] confirm that the precursor cuboids crystallized in the hydrate phase $NiMoO_4$•nH_2O with a triclinic unit cell (space group P-1), which is different to the monoclinic α and β-$NiMoO_4$ phases existing under atmospheric pressure (space group C12/m1).

The determined Mo-L_{II} and Mo-L_{III} absorption edges of MoO_2/$MoNi_4$ (Figure 4, red graph) consist of a superposition of spectra generated from MoO_2 (oxidation state 4+) and $MoNi_4$ (intermetallic compound). The broad peaks at the Mo-L_{II} and Mo-L_{III} edges include no resonance peaks, which indicates the superposition of two metal-like spectra from "metallic" MoO_2 and from the intermetallic phase $MoNi_4$ (mainly metallic bonding with ionic contributions). This observation confirms XRD and TEM data of this sample that the Mo oxide investigated is metallic MoO_2, a rutile-like structure with a monoclinic unit cell (space group $P2_1/c$).[18,28] It is also in line with NEXAFS studies at the Mo-L_{III} edge of MoO_3 (double peak) and MoO_2 (one broad peak) published by Hara et al[30] and Lede et al.[31]

In sum, the NEXAFS-TXM data demonstrate a complete conversion of $MoNiO_4$ into MoO_2 cuboids and the formation of electrocatalytically active $MoNi_4$ nanoparticles. Further investigations might include operando studies of kinetic processes and NEXAFS investigations of individual $MoNi_4$ nanoparticles with even higher spatial resolution. In addition, since synchrotron radiation is inherently highly polarized, X-ray dichroism could be explored to gather a deeper understanding of crystalline orientations in $MoNi_4$ catalysts. The capabilities to study dichroic materials using NEXAFS-TXM have been demonstrated by Guttmann et al.,[2] Krüger et al.[32] as well as Bittencourt et al.[33] An elliptical in-vacuum undulator device allowing full polarization control combined with the presented ML blazed PGM setup will permit dichroism studies in the tender X-ray regime in the near future.

In microelectronics, silicon plays an important role since different dielectrics containing silicon are used as insulating materials in on-chip interconnect stacks of advanced integrated circuits (IC). To increase the performance of advanced microelectronic devices, conventional silicon oxide (SiO_2) has been substituted by organosilicate glass (OSG) with low dielectric permittivity, and silicon carbon nitrides (SiCN) are used as an etch stop layer in the patterning process (see Figure S13, Supporting Information). The challenge is to balance dielectric and mechanical properties of these nanostructured layer stacks, which can be tuned by the chemical bonding of the insulating thin film materials and further optimized by the geometrical arrangement of the metal interconnects. NEXAFS spectromicroscopy at the Si-K absorption edge, combining high lateral and spectral resolution, yields the chemical bonding in different types of dielectrics in the nanopatterned interconnect stack.

In X-ray spectromicroscopy, the quality of the NEXAFS spectrum derived from an image series taken within a photon energy range is directly linked to the signal-to-noise ratios in the single images. The photon flux increase of the ML-PGM over the Au-PGM should also be reflected by the effective exposure times required for imaging in the TXM. Both monochromator setups were used to take images of different IC samples with the TXM. With the Au-PGM, the exit slit width and the exposure times were increased until similar image qualities were obtained compared to the images acquired with the ML-PGM. The respective exit slit width (ESW) multiplied by the exposure time (t_{exp}) of the two monochromators results in the factor by which the photon flux in the ML-PGM is higher. As shown in **Figure 5**, the photon flux increase is slightly more than two-orders-of-magnitude at 2.5 keV, independent of the sample thickness. Around the Si-K edge, the photon flux increase is more than one-order-of-magnitude. These results are in good agreement with the photon flux measurements shown in Figure 2. In general, high-resolution imaging strongly benefits from short exposure times, since degradation of the image quality due to sample drift or instabilities in the optical setup is much reduced. Moreover, the operation with small exit slit width is desirable to provide maximum spectral resolution.

In addition, we investigated the effect of the number of photons used for imaging on the quality of the NEXAFS spectra, in particular the noise level (see Figure S14, Supporting Information). Another parameter influencing the signal-to-noise ratio in the NEXAFS spectra is the sample thickness.

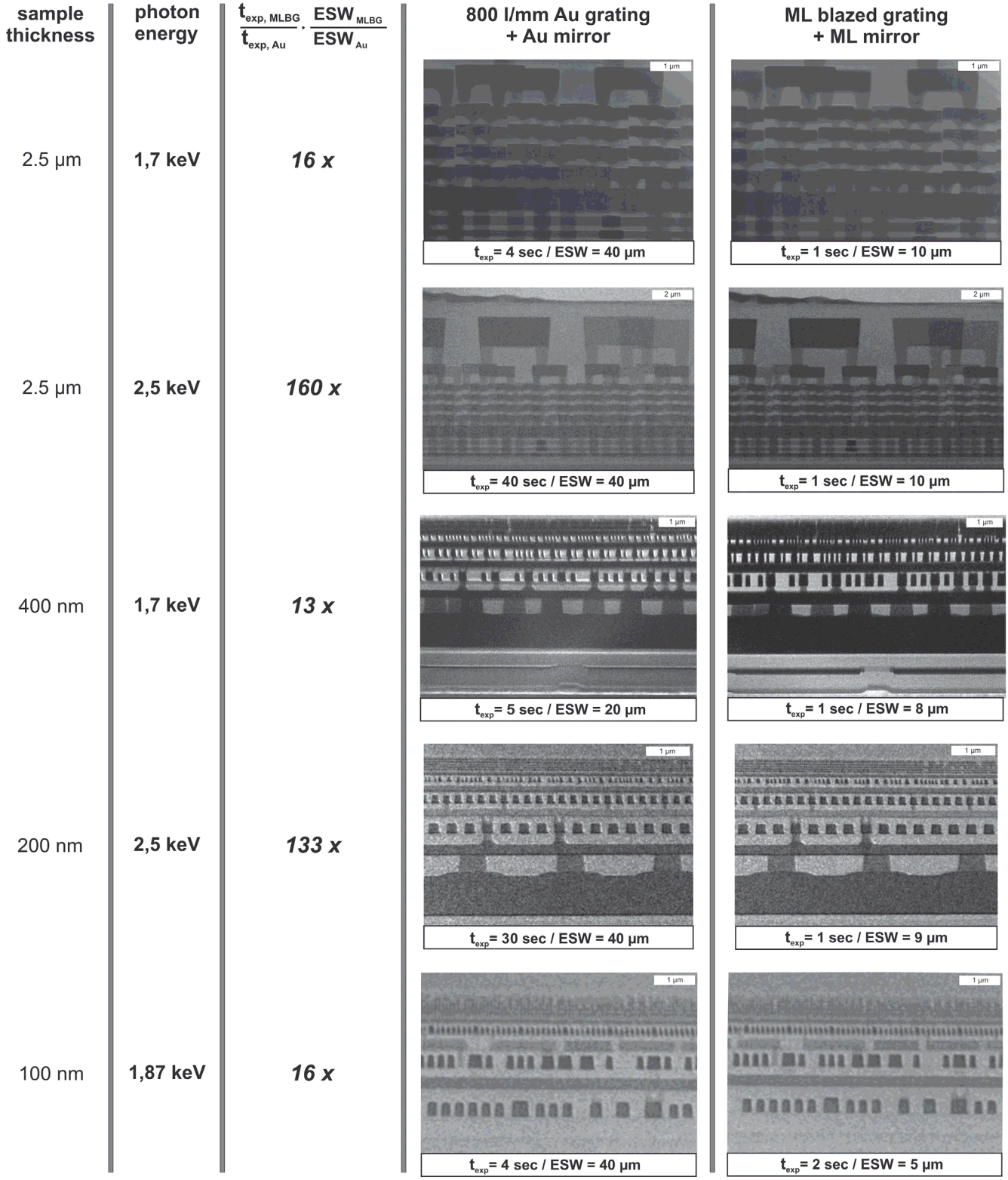

Figure 5. Comparison of TXM images of IC samples with different thicknesses (100, 200, 400 nm, and 2.5 µm) acquired at photon energies around the Si-K absorption edge and 2.5 keV. The images show recordings of the IC structures with the Au-PGM (left column) and the ML-PGM (right column). In order to obtain similar image qualities, we found that the exposure times (t_{exp}) and the exit slit widths (ESW) had to be significantly larger to compensate for the much less efficient Au-PGM setup. Moreover, the images taken using the ML-PGM seem to have an improved image contrast.

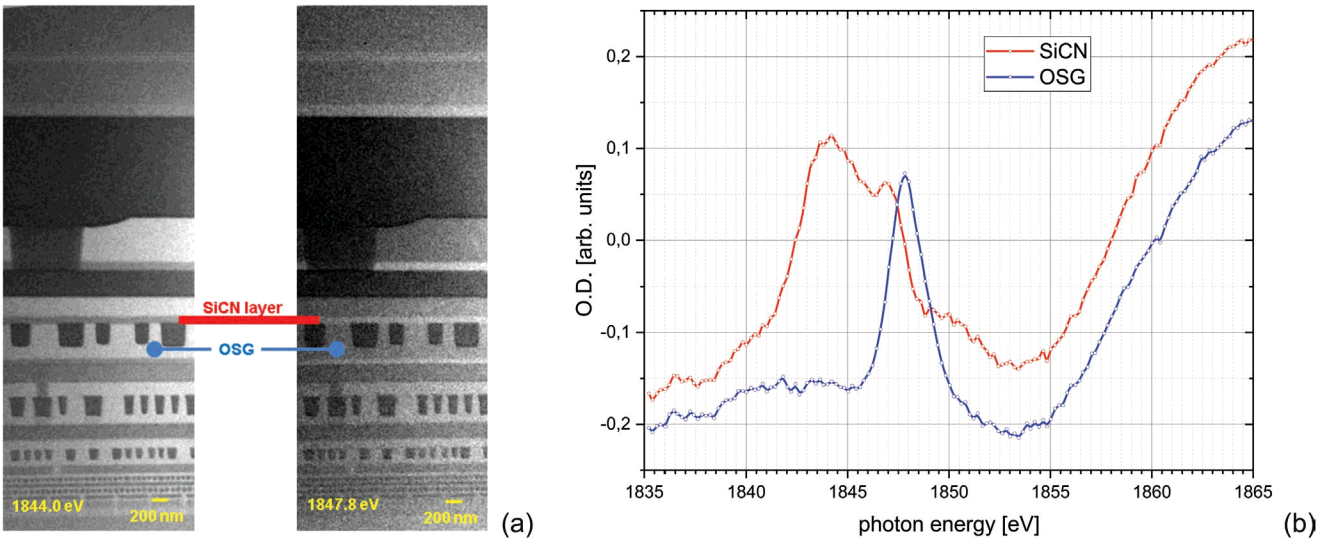

Figure 6. a) TXM images (3rd order imaging) of a 400 nm thick lamella cut out of an IC interconnect stack. The images were taken from an energy series at the Si-K absorption edge. b) Corresponding NEXAFS spectra extracted from the acquired energy series for SiCN and OSG materials. The corresponding energy peaks are related to the dominating Si—C bonds for SiCN and the dominating Si—O bonds for OSG dielectrics.

We tested different sample thicknesses, and found that the IC lamellas with 400 nm thickness offer the best compromise between an optimized image contrast and a sufficient signal-to-noise level for the NEXAFS analysis at the Si-K absorption edge. **Figure 6**a shows TXM images acquired at 1844.0 and 1847.8 eV of such a 400 nm thick lamella cut from an IC manufactured in an advanced CMOS technology node with an interconnect stack consisting of 12 layers of copper. Local NEXAFS spectra at the Si-K-edge were measured from two nano-size marked regions: SiCN (red) and porous OSG (blue) (see Figure 6a,b). We obtained for SiCN (red) an energy peak at 1842.5 eV and for OSG (blue) at 1847.0 eV. These energies are related to the dominating Si-C bonds for SiCN and the dominating Si—O bonds for OSG dielectrics.

The OSG has mainly small angle/network Si—O—Si bonds, and in addition Si—OH and Si—CH_3 bonds (based on FTIR and ^{29}Si NMR studies).[34] The energy difference of 4.5 eV also confirms the expected shift of the Si-K absorption edge to higher photon energies for increasing O coordination and decreasing C coordination and is in agreement with reported measurements for SiC and OSG.[34–36] In addition, a broadened resonance peak in the Si-K NEXAFS spectrum for the SiCN region is observed. This most likely reflects a double peak corresponding to anti-bonding Si 3p–N 2p and Si 3p–C 2sp hybridized states,[35] as the broadening was well fit by two Gaussian functions with an energy difference of 2.9 eV (Figures S15 and S16, Supporting Information).

4. Conclusion

We have shown that the gain of two orders of magnitude in photon flux in the tender photon energy range enabled by our novel ML-PGM setup permits determination of the electronic states of hierarchically nanostructured materials from both energy technologies and microelectronics. Thus, with our new setup many more artificial and natural materials containing elements with absorption edges in the tender X-ray regime become accessible for a combined structural and electronical analysis under significantly improved experimental conditions. Our finding that the monochromator is about two orders of magnitude more efficient than conventional solutions makes this optical setup superior for the tender photon energy range 1.5–5 keV (or even higher up to 10 keV). Therefore, we expect that this monochromator setup will become the method of choice for imaging in the tender X-ray photon energy range not only at synchrotrons worldwide, but also with free electron lasers (FEL's) and laboratory sources. Single shot experiments with FEL's or laboratory high harmonic generation (HHG) sources will dramatically benefit from two orders of magnitude more photons. Also classical X-ray tube experiments requiring a small energy bandwidth will have substantial shorter exposure times. All of this demonstrates the importance of this novel monochromator concept for modern technologies with all their key elements in the tender X-ray regime. This applies not only at large-scale facilities, but also at different types of laboratory sources, which are widely used for many imaging and spectroscopic applications in science and industry. In other cases, like RIXS (resonant inelastic X-ray scattering) experiments, this monochromator can be utilized as an analyzer monochromator resulting in 100-fold less radiation damage to the sample, plus shorter exposure times. Additionally, the combination of our approach with further gains provided by the higher brilliance of 4th generation light sources that are coming to life will enable the exploration of previously unattainable scientific questions.

5. Experimental Section

For the experiments in the tender photon energy range, a multilayer coated blazed grating in combination with a multilayer coated plane mirror was manufactured, and is now installed at the X-ray microscopy beamline U41-PGM1-XM at the BESSY-II electron storage ring. The ML

grating is based on a mechanically ruled[37] blazed grating with a line density of 2000 lines mm^{-1} fabricated on a 100 mm long plane super polished substrate. The blazed grating as well as the super polished pre-mirror of 310 mm in length (both show a micro-roughness of ≤0.2 nm rms and a slope error of ≤250 nrad rms) have been coated with 30 bilayers of Cr/C-multilayer in one deposition sequence at the same time by means of direct current magnetron sputter technology at Tongji University (see Figure S1; Supporting Information).[38] Further details of the ML deposition process are in the Supporting Information. All other mirrors in the beamline are coated with Rh and have a grazing incidence angle of 1° to provide a high reflectivity up to a photon energy of 3 keV.

In order to demonstrate experimentally the advantage of the ML coated in comparison to the conventional Au coated optics, we exchanged only the two pairs of optical elements without changing any of the other beamline mirrors. The photon flux was measured in front of the TXM at a distance of 9 m from the monochromator exit slit using a GaAsP-diode with a 2 mm diameter aperture. In a first alignment step, the angles β and θ for the ML-PGM setup were chosen according to values determined by at-wavelength pre-measurements of the efficiency and reflectivity of the individual optical elements at the BESSY-II optics-beamline[39] and PTB-KMC at BESSY-II[40] (Figures S3–S5; Supporting Information). Furthermore, we optimized the photon flux for photon energies in the tender X-ray range by matching these angles to values calculated by raytracing simulations, resulting in a well-defined energy calibration for the ML coated PGM setup. In addition, the gap of the U41 undulator was optimized at each photon energy. The undulator was used in the 3rd harmonic for 700–1000 eV, in the 5th harmonic for 1000–1700 eV and in the 9th harmonic for 1700–3500 eV photon energies, respectively. The monochromator exit slit width was set to 20 µm.

The NEXAFS spectra for the $NiMoO_4$ and for $MoO_2/MoNi_4$ studies were extracted from TXM image sequences acquired in the photon energy range covering the corresponding Mo-L_{III} and Mo-L_{II} absorption edges using the monochromator setup based on ML coated optics at the U41-PGM1-XM beamline at BESSY-II. The TXM was equipped with a zone plate objective with 25 nm outermost zone width,[41] and the monochromator exit slit width was 7 µm for $NiMoO_4$ and 5 µm for $MoO_2/MoNi_4$, respectively. The exposure time was set to 2 s per image. The IC interconnect stacks were imaged with the same zone plate objective, a monochromator exit slit width of 20 µm and 5 s exposure time per image.

Supporting Information

Supporting Information is available from the Wiley Online Library or from the author.

Acknowledgements

The authors thank the Helmholtz-Zentrum Berlin für Materialien und Energie for the allocated beam time and experimental support at BESSY-II. They also thank Jens Viefhaus, Karsten Holldack, and James McNally, Helmholtz-Zentrum Berlin, Germany, Francesca Iacopi, University of Technology Sydney, Australia, and Juris Purans, University of Riga, Latvia, for fruitful discussions as well as Yvonne Standke, Fraunhofer IKTS Dresden, Germany, for sample preparation and Stefan Rehbein, Helmholtz-Zentrum Berlin, Germany, for the development and manufacturing of the high resolution transmission zone plate optics required for the operation of the HZB-TXM.

Open access funding enabled and organized by Projekt DEAL.

Conflict of Interest

The authors declare no conflict of interest.

Author Contributions

G.S. and R.F. developed the conceptional idea to use multilayer optics for the tender X-ray photon energy range beamline. F.S., R.F., S.W., and P.G. simulated the required parameters of the multilayer blazed grating and mirror for operation in the U41-PGM1 beamline. Q.H., Y.F., T.L., Z.W., and F.S. were responsible for the fabrication of the multilayer optics. F.S. and A.S. characterized the optical properties of the multilayer blazed grating and mirror. M.M. and P.G. installed and adjusted the multilayer optics at U41-PGM1 beamline. P.G. and S.W. did the commissioning tasks at wavelength with multilayer and standard plane optics at U41-PGM1 beamline. S.W. and P.G. performed the imaging and spectromicroscopy investigations on the catalytic and microelectronic samples and did the data analysis. Z.L., K.K., J.Z., X.F., and E.Z. prepared the catalytic and microelectronic samples and contributed to the data interpretation. S.W., P.G., E.Z., and G.S. wrote the article. All authors have given approval to the final version of the manuscript.

Data Availability Statement

The data that support the findings of this study are available from the corresponding author upon reasonable request.

Keywords

blazed multilayer grating, catalysts, dielectrics, electrochemical energy conversion, microelectronics, tender X-ray energy range, X-ray spectromicroscopy

Received: October 25, 2022
Published online:

[1] R. Follath, F. Senf, *ScienceDirect* **1997**, *390*, 388.
[2] H. Petersen, H. Baumgärtel, *Nuclear Instruments and Methods* **1980**, *172*, 191.
[3] J. H. Beaumont, M. Hart, *J. Phys. E: Sci. Instrum.* **1974**, *7*, 823.
[4] A. M. Maiden, G. R. Morrison, B. Kaulich, A. Gianoncelli, J. M. Rodenburg, *Nat. Commun.* **2013**, *4*, 1669.
[5] P. Guttmann, C. Bittencourt, S. Rehbein, P. Umek, X. Ke, G. Van Tendeloo, C. P. Ewels, G. Schneider, *Nat. Photon* **2012**, *6*, 25.
[6] G. Schneider, P. Guttmann, S. Heim, S. Rehbein, F. Mueller, K. Nagashima, J. B. Heymann, W. G. Muller, J. G. McNally, *Nat. Methods* **2010**, *7*, 985.
[7] F. Senf, F. Bijkerk, F. Eggenstein, G. Gwalt, Q. Huang, R. Kruijs, O. Kutz, S. Lemke, E. Louis, M. Mertin, I. Packe, I. Rudolph, F. Schäfers, F. Siewert, A. Sokolov, J. M. Sturm, C. Waberski, Z. Wang, J. Wolf, T. Zeschke, A. Erko, *Opt. Express* **2016**, *24*, 13220.
[8] A. Sokolov, Q. Huang, F. Senf, J. Feng, S. Lemke, S. Alimov, J. Knedel, T. Zeschke, O. Kutz, T. Seliger, G. Gwalt, F. Schäfers, F. Siewert, I. V. Kozhevnikov, R. Qi, Z. Zhang, W. Li, Z. Wang, *Opt. Express* **2019**, *27*, 16833.
[9] Q. Huang, I. V. Kozhevnikov, A. Sokolov, Y. Zhuang, T. Li, J. Feng, F. Siewert, J. Viefhaus, Z. Zhang, Z. Wang, *Opt. Express* **2020**, *282*, 821.
[10] P. Guttmann, S. Werner, F. Siewert, A. Sokolov, J.-S. Schmidt, M. Mast, M. Brzhezinskaya, C. Jung, R. Follath, G. Schneider, *Microsc. Microanal.* **2018**, *24*, 204.
[11] G. Schneider, *Ultramicroscopy* **1998**, *75*, 85.
[12] F. Schäfers, in, (Eds.: A. Erko, M. Idir, T. Krist, A. G. Michette), Springer, Berlin, Heidelberg **2008**.
[13] J. Bahrdt, *Appl. Opt.* **1997**, *36*, 4367.
[14] J. Bahrdt, W. Frentrup, S. Grimmer, C. Kuhn, C. Rethfeldt, M. Scheer, B. Schulz, **2018**.

[15] E. Pomerantseva, F. Bonaccorso, X. Feng, Y. Cui, Y. Gogotsi, *Science* **2019**, *366*, eaan8285.
[16] R. F. Egerton, *Electron Energy-Loss Spectroscopy in the Electron Microscope*, Springer, Berlin **2011**.
[17] E. Topal, Z. Liao, M. Löffler, J. Gluch, J. Zhang, X. Feng, E. Zschech, *BMC Materials* **2020**, *2*, 5.
[18] J. Zhang, T. Wang, P. Liu, Z. Liao, S. Liu, X. Zhuang, M. Chen, E. Zschech, X. Feng, *Nat. Commun.* **2017**, *8*, 15437.
[19] J. A. Rodriguez, S. Chaturvedi, J. C. Hanson, A. Albornoz, J. L. Brito, *J. Phys. Chem. B* **1998**, *102*, 1347.
[20] D. O. Scanlon, G. W. Watson, D. J. Payne, G. R. Atkinson, R. G. Egdell, D. S. L. Law, *J. Phys. Chem. C* **2010**, *114*, 4636.
[21] K. Inzani, M. Nematollahi, F. Vullum-Bruer, T. Grande, T. W. Reenaas, S. M. Selbach, *Phys. Chem. Chem. Phys.* **2017**, *19*, 9232.
[22] A. Bolzan, B. Kennedy, C. Howard, *Aust. J. Chem.* **1995**, *48*, 1473.
[23] L. Lajaunie, F. Boucher, R. Dessapt, P. Moreau, *Ultramicroscopy* **2015**, *149*, 1.
[24] S. Chaturvedi, J. A. Rodriguez, J. L. Brito, *Catal. Lett.* **1998**, *51*, 85.
[25] K. O. Hodgson, B. Hedman, J. E. Penner-Hahn, *EXAFS and Near Edge Structure*, Springer, Berlin **1984**.
[26] K. Eda, Y. Kato, Y. Ohshiro, T. Sugitani, M. S. Whittingham, *J. Solid State Chem.* **2010**, *183*, 1334.
[27] A. P. de Moura, L. H. de Oliveira, I. L. V. Rosa, C. S. Xavier, P. N. Lisboa-Filho, M. S. Li, F. A. La Porta, E. Longo, J. A. Varela, *Sci. World J.* **2015**, *2015*.
[28] Y.-Y. Chen, Y. Zhang, X. Zhang, T. Tang, H. Luo, S. Niu, Z.-H. Dai, L.-J. Wan, J.-S. Hu, *Adv. Mater.* **2017**, *29*, 1703311.
[29] W. Du, Y. Shi, W. Zhou, Y. Yu, B. Zhang, *Angew. Chem., Int. Ed.* **2021**, *60*, 7051.
[30] D. Hara, H. Ikuta, Y. Uchimoto, M. Wakihara, *J. Mater. Chem.* **2002**, *12*, 2507.
[31] E. J. Lede, F. G. Requejo, B. Pawelec, J. L. G. Fierro, *J. Phys. Chem. B* **2002**, *106*, 7824.
[32] P. Krüger, M. Sluban, P. Umek, P. Guttmann, C. Bittencourt, *J. Phys. Chem. C* **2017**, *121*, 17038.
[33] C. Bittencourt, S. Werner, C. Haebel, P. Guttmann, M. Sluban, P. Umek, P. Kruger, *Microsc. Microanal.* **2018**, *24*, 474.
[34] F. Iacopi, G. Beyer, Y. Travaly, C. Waldfried, D. M. Gage, R. H. Dauskardt, K. Houthoofd, P. Jacobs, P. Adriaensens, K. Schulze, S. E. Schulz, S. List, G. Carlotti, *Acta Mater.* **2007**, *55*, 1407.
[35] Y. K. Chang, H. H. Hsieh, W. F. Pong, M. H. Tsai, T. E. Dann, F. Z. Chien, P. K. Tseng, L. C. Chen, S. L. Wei, K. H. Chen, J. J. Wu, Y. F. Chen, *J. Appl. Phys.* **1999**, *86*, 5609.
[36] A. Grill, S. M. Gates, T. E. Ryan, S. V. Nguyen, D. Priyadarshini, *Appl. Phys. Rev.* **2014**, *1*, 011306.
[37] F. Siewert, B. Lochel, J. Buchheim, F. Eggenstein, A. Firsov, G. Gwalt, O. Kutz, S. Lemke, B. Nelles, I. Rudolph, F. Schafers, T. Seliger, F. Senf, A. Sokolov, C. Waberski, J. Wolf, T. Zeschke, I. Zizak, R. Follath, T. Arnold, F. Frost, F. Pietag, A. Erko, *J Synchrotron Radiat* **2018**, *25*, 91.
[38] H. Ni, Q. Huang, Y. Shi, R. Qi, Z. Zhang, Y. Feng, X. Xu, Z. Zhang, J. Wang, Z. Li, *Optical Engineering* **2019**, *58*, 104105.
[39] F. Schäfers, P. Bischoff, F. Eggenstein, A. Erko, A. Gaupp, S. Künstner, M. Mast, J. S. Schmidt, F. Senf, F. Siewert, A. Sokolov, T. Zeschke, *J Synchrotron Radiat* **2016**, *23*, 67.
[40] M. Krumrey, G. Ulm, *Nucl. Instrum. Methods Phys. Res., Sect. A* **2001**, *467*, 1175.
[41] S. Rehbein, S. Heim, P. Guttmann, S. Werner, G. Schneider, *Phys. Rev. Lett.* **2009**, *103*, 110801.